Direct Amplitude Control for Voice Coil Motor on High Frequency Reciprocating Rig

Ruotong Wang, Xin Yin, Qibing Wang, and Lin Jiang, *Member, IEEE*

***Abstract*—High frequency reciprocating rig (HFRR) that utilises direct drive voice coil motor (VCM) is designed to perform pin-on-flat tribotest such as assessing the lubricity of fuel. In this paper, we propose direct amplitude control to maintain the amplitude of high frequency reciprocating motion of VCM on HFRR subjects to frictional load. First, the mathematical model of HFRR is developed, which takes the effect of frictional load into consideration. Subsequently, direct amplitude control is proposed, which takes the error of amplitude rather than position error as performance index. It consists of an amplitude regulator and an offset compensator. Analysis and simulations of the proposed control method are presented as well. Finally, the proposed control method is deployed to a digital signal processor on an HFRR prototype experimental platform. The experiment results indicate a significant improvement of the performance of VCM based HFRR in terms of amplitude accuracy in high frequency band compared with that given by traditional PI control. The results also suggest the instability of PR control in this case.**

***Index Terms*—Friction, motion control, voice coil motor(VCM)**

I. Introduction

FRICTION and wear in manufacturing and transportation lead to considerable losses. It is estimated that 25% of the energy input in industry is spent on overcoming friction forces. On a large scale, the losses connected with friction and wear in machines are estimated in 3% to 5% of the gross national product [1]. Thus, the industrial significance of tribological study of phenomena of friction and wear has long been recognised by researchers [2]. As the interactions between surfaces are influenced by not only the materials couple but also the characteristics of the whole tribosystem. Therefore, tribological properties that follow the systems aspect of friction and wear call for tribotest in the process of tribological study [3]. A number of friction and wear test apparatuses have been developed for different tribological applications, and can be classified according to their interface geometries, such as pin-on-disk, pin-on-flat, pin-on-cylinder, etc.

In this paper, we focus on a test apparatus applied in pin-on-flat tribotest called high frequency reciprocating rig (HFRR). On HFRR, a flat moves relative to a stationary pin in reciprocating motion [2]. It is usually driven by voice coil motor (VCM) at high frequency with a small amplitude. VCM is a direct drive DC motor with its structure similar to that of a loudspeaker. It can offer unlimited high resolution due to the absence of commutation and transmission device, which is attractive to the applications that requires accurate positioning and fast response [4]. It has been widely used in precision positioning and vibration isolation applications [5] [6]. However, according to HFRR standard [7], the relative errors of the results obtained by commercial VCM based HFRR can be more than 30%. One reason of such large error is that during the time of operation, the coefficient of friction keeps on changing, which contributes to the non-linearity and time-dependent characteristics of the system. In addition, the sinusoidal position trajectory required by standard ISO-12156-1:2016 will lead to periodic zero-crossing of velocity. Therefore, the friction exerts on motor shaft can change abruptly at those points due to the transitions between kinetic friction and static friction (slip-stick effect), which makes the position control problem challenging. As a result, friction as a typical hard nonlinear disturbance leads to the difficulty in VCM position control [8] [9]. Consequently, there is a need to improve the performance of HFRR in the application of pin-on-flat tribotest, which relies on the control of VCM on HFRR.

As a widely used model-free approach, PID control has been adapted to VCM position control. [10] suggests that the gains of PID controller applied to VCM position control can be tuned online by fuzzy logic technique. [11] modifies conventional PID to state feedback style position velocity controller with disturbance observer. Both [12] and [13] investigate the application of nonlinear PID technique on VCM. All controllers aforementioned target to control the real-time position to track a given sinusoidal reference. However, the control objective of a VCM based HFRR is to maintain a constant magnitude of the position signal at high frequency oscillation, rather than to drive the position signal to track the reference in real time. This is required in the assessment standard ISO-12156-1:2016 [7].Based on author's best knowledge, there is no controller design published to directly regulate the magnitude of the position signal of VCM.

This paper proposes direct amplitude control of the position of VCM based HFRR. The structure of this paper is organised as follows. Section II presents the development of the mathematical model of VCM based HFRR, which can be separated into VCM model and frictional load model. In section III, we propose a novel controller called direct amplitude control, it takes the amplitude rather than position as performance index to achieve amplitude regulation of VCM. Simulations and experiments to verify the proposed control method are

Ruotong Wang and Xin Yin and Lin Jiang are with the Department of Electrical Engineering and Electronics, the University of Liverpool, Liverpool, UK, L69 3GJ (email: rw2016@liverpool.ac.uk; Xin.Yin@liverpool.ac.uk; ljiang@liv.ac.uk)

Qibing Wang (corresponding author) is with Sicher Elevator Co., Ltd. No.1 Sicher Rd, Lianshi Industrial Park, Huzhou City, Zhejiang, China (email: 43410697@qq.com)

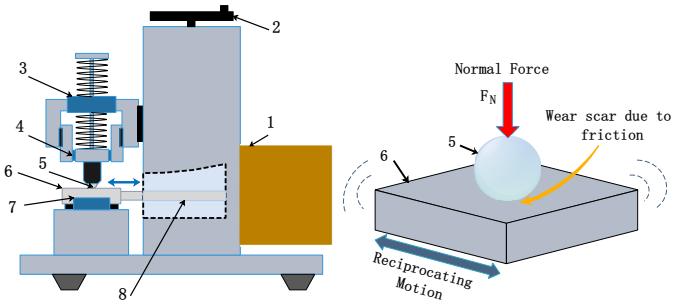

(a) Schematic of HFRR (b) Operation principle

Fig. 1: Schematic and operation principle of HFRR: 1) Voice Coil Motor, 2) Normal Force Adjustment, 3) Normal Force Sensor, 4) Friction Sensor, 5) Test Ball, 6) Test Plate, 7) Incremental Encoder, 8) Motor Shaft

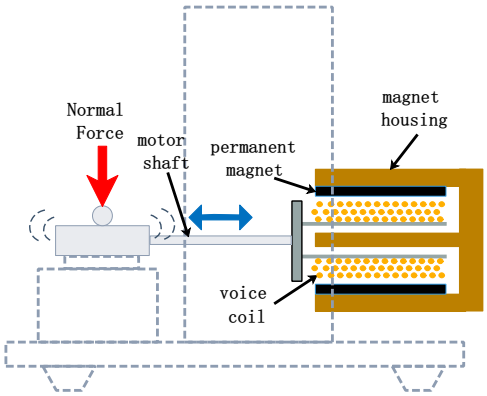

Fig. 2: Schematic of VCM on HFRR: the test plate is directly connected to the voice coil of VCM through shaft.

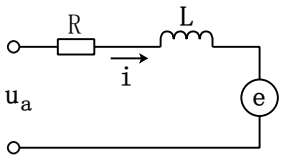

Fig. 3: Electric circuit model of VCM

shown in section IV. The comparisons among the proposed control method, PR control and conventional PI control are presented as well. Section V concludes this paper.

II. Mathematical Model of HFRR

A. Operation of HFRR

HFRR has been widely used to conduct pin-on-flat tribotest, where a flat component is driven by the testing rig to achieve high frequency reciprocating motion with respect to a pin or ball component. Fig. 1.(a) shows the schematic of the HFRR. The operation of HFRR is shown inFig. 1.(b).When conducting the experiment, the test plate oscillates at a fixed frequency with a fixed stroke. In the meantime, the normal force is exerted to push the test ball against the test plate. Usually, the test ball is loaded against the test plate with a fixed force during experiment. The contact interface is immersed in a fluid. The friction between the test ball and test plate directly exerts on the coil of VCM through motor shaft. After the operation of the test, the test ball together with the ball holder should be removed from the rig. The diameter of the wear scar on the contacting surface of test ball can be measured through microscope.

A typical application is the assessment of the lubricity of diesel fuel. Diesel fuel acts as a lubricant in all diesel fuel injection equipment. [7] presents a standard method to assess the lubricity of diesel fuel. The idea is to realise the relative motion between a steel ball and a steel plate that contact with each other. The steel plate immerses in the diesel fuel. By examining the diameter of wear scar on the steel ball after the experiment, the lubricities of different diesel fuels can be assessed.

Fig. 2 shows the structure of the voice coil motor on HFRR, which mainly consists of permanent magnet and voice coil. The load is connected to the voice coil through motor shaft. As the friction exerts on the coil of VCM through motor shaft, the model of HFRR is obtained by combining VCM model and frictional load model.

B. Model of VCM

As VCM is a DC motor, the attributes of a VCM are similar to that of a generalised DC motor with permanent magnet. Fig. 3 depicts the equivalent circuit for VCM. The impedance of voice coil is represented in the form of a resistor and inductor in series. In addition, the back electromotive force due to electromagnetic induction on moving coil is demonstrated as a voltage source. According to the Kirchhoff's Circuit Law, (1) holds. u_a is the voltage between the terminals of VCM. i is the current flows into the coil. R and L are resistance and inductance of the equivalent circuit. e is counter-Electro-Motive Force (counter EMF).

$$u_a = e + iR + L\dot{i} \tag{1}$$

When operating VCM, the desired amplitude of oscillation of the voice coil is usually less than $1mm$, which is small compared with the length of the air gap. The length of that applied in our research is $110mm$. Therefore, the magnetic field flux density is treated as a constant lumped parameter, as the distributed attribute of it can be ignored in the case of such small amplitude of oscillation. In addition, the effective length of the coil that generating Lorentz force is the same as the total length of the voice coil, since the full length of voice coil subjects to the magnetic field in air gap during its oscillation. The counter EMF can be derived as:

$$e = Blv \tag{2}$$

B is the magnetic field flux density in the air gap. l is the total length of the coil. v is the velocity of the moving coil. It can be found that considering all the variables in the equation of counter EMF, only the velocity of the coil can be changed in the operation of the motor. Therefore, we define the product of B and l as motor constant.

$$K_s = Bl \tag{3}$$

Fig. 4 presents the mechanical characteristics of VCM. Previous study [15] indicates that there are two types of VCM,

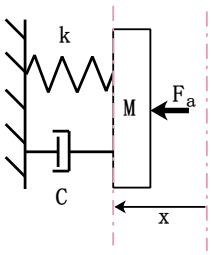

Fig. 4: Analytic mechanical model of VCM [14]

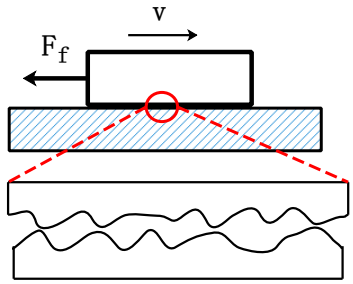

Fig. 5: Basic friction configuration with enlarged contacting surfaces [17]

namely MFK type and MF type. MFK type VCM deploys a spring to support the moving coil. In this paper, we only consider MFK type linear VCM. In Fig. 4, k represents spring factor. C is damping factor. M is the total mass of the moving part of VCM. In addition, x is the displacement of VCM shaft. According to Newtons Laws of Motion, we can obtain the following equation:

$$M\ddot{x} + C\dot{x} + kx = F_a \tag{4}$$

where F_a is the Ampere's force given by:

$$F_a = K_s i \tag{5}$$

Rearrange (1) to (5) above, we can derive the mathematical model of VCM:

$$\begin{cases} \dot{x} = v \\ \dot{v} = -\frac{k}{M} \cdot x - \frac{C}{M} \cdot v + \frac{K_s}{M} \cdot i \\ \dot{i} = -\frac{K_s}{L} \cdot v - \frac{R}{L} \cdot i + \frac{1}{L} \cdot u_a \end{cases} \tag{6}$$

C. Model of Frictional Load

Friction is a common phenomenon which can be defined as the resistance to motion when two surfaces slide against each other [16]. Fig. 5 shows the lumped forces that exist in a tribological system. v is the velocity of relative motion of the upper body with respect to the lower body. F_f is the friction force in the reverse direction of motion. The enlarged contacting surfaces in Fig. 5 show their geometries at the microscopic level. There is a large number of asperity junctions that exist on two contacting surfaces, which contribute to the origin of friction [17].

Previous research reveals that two friction regimes can be defined in the sliding process of a tribological system, namely, the pre-sliding regime and the gross sliding regime [18] [19]. By taking both pre-sliding regime and gross sliding regime into account, LuGre model is raised, which is depicted in Fig. 6. LuGre model takes the average behaviour of the bristles that represent the deformations of asperity junctions as a state variable [20]. It is capable of capturing several effects such as stick-slip oscillations and zero-slip displacement [21]. In Fig. 6, z denotes the average deflection of bristles, which is modelled as:

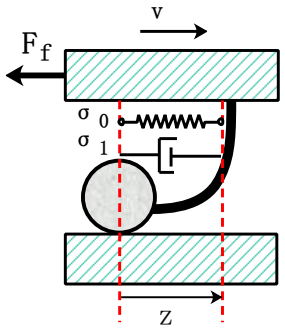

Fig. 6: LuGre model [16]

$$\dot{z} = v - \sigma_0 \frac{|v|}{S(v)} z \tag{7}$$

where v is velocity, σ_0 is asperity stiffness, $S(v)$ is a function of sliding velocity that accounts for the Stribeck effect [22]:

$$S(v) = F_c + (F_s - F_c) e^{-(|\frac{v}{v_s}|)^{\sigma_{vs}}} \tag{8}$$

where F_c and F_s stand for the Coulomb friction force and Static friction force respectively, v_s is Stribeck velocity, and σ_{vs} is the shape factor that determines the shape of Stribeck curve. According to the configuration of LuGre Model, the component of friction force due to bristle effect is given by:

$$F_{bristle} = \sigma_0 z + \sigma_1 \dot{z} \tag{9}$$

where σ_0 and σ_1 represent the asperity stiffness and damping coefficient of frictional interface respectively. To consider the effect of viscous friction, a term proportional to the sliding velocity is added [23] and the lumped friction force is obtained as:

$$F_f = F_{bristle} + \sigma_2 v \tag{10}$$

Finally, the detailed LuGre model is summarised as:

$$\begin{cases} F_f = \sigma_0 z + \sigma_1 \dot{z} + \sigma_2 v \\ \dot{z} = v - \sigma_0 \frac{|v|}{S(v)} z \\ S(v) = F_c + (F_s - F_c) e^{-(|\frac{v}{v_s}|)^{\sigma_{vs}}} \end{cases} \tag{11}$$

D. Model of HFRR

As it can be seen from figure 1, there is no gearbox installed between the load and the motor shaft. The VCM in operation subjects to the frictions that arise from two tribosystems, which are the contacting surfaces between the test ball and the test plate and the linear guide that supports the test plate. It is noted that the friction arises from the linear guide is in the same direction as that between the test ball and the test plate. Therefore, they are treated as a lumped friction exerts on VCM in modelling. The model of HFRR can be obtained by

combining model of VCM and that of frictional load together. Finally, the model of HFRR is:

$$\begin{cases} \dot{x} = v \\ \dot{v} = -\frac{k}{M} \cdot x - \frac{C}{M} \cdot v + \frac{K_s}{M} \cdot i - \frac{1}{M} \cdot F_f \\ \dot{i} = -\frac{K_s}{L} \cdot v - \frac{R}{L} \cdot i + \frac{1}{L} \cdot u_a \end{cases} \tag{12}$$

where the expression of frictional load F_f can be found in (11). In general, the developed model of HFRR suggests a 4^{th} order nonlinear system. x is the output of the system, which is the position signal of motor shaft. u_a is the input of the system, which is the voltage applied to VCM.

III. Control Design and Analysis

A. PI Control

The position control of motor is usually regarded as a reference tracking problem, of which the aim is to minimise the error between the measured position signal and reference signal. The most popular controller is PI controller, which is shown in (13):

$$G_{pi}(s) = k_p + \frac{k_i}{s} \tag{13}$$

where k_p and k_i are proportional gain and integral gain.

B. PR Control

A conventional PI controller in stationary reference frame can lead to steady state amplitude and phase error when tracking a sinusoidal reference [24]. According to internal model principle, a compensator with a sinusoidal transfer function can be applied to the system in this situation [25]. It has been proved that the steady state error can be zero once the closed system is asymptotically stable. The transfer function of the controller is shown in (14). It consists of a proportional term and a resonant term.

$$G_{pr}(s) = k_p + \frac{k_i \cdot s}{s^2 + \omega_0^2} \tag{14}$$

ω_0 is the angular frequency of the sinusoidal reference. k_p and k_i are proportional gain and resonant gain.

C. Direct Amplitude Control

Recall the operation of HFRR, which requests maintain a constant amplitude of vibration at the desired frquency and small midpoint offset during experiments. The phase of the position signal is of no concern in application. Therefore, the proposed control method is designed to achieve the following aims:

1) Maintain constant amplitude of vibration
2) Maintain constant frequency of vibration
3) Suppress DC component (offset of midpoint)

The basic idea is to adjust the amplitude of the position signal by varying the amplitude of sinusoidal voltage signal applied between the terminals of VCM. In addition, a varying DC voltage is applied to fight against the drift of midpoint of the position signal. According to the results of the open loop response test of HFRR, the fundamental frequency of output signal is the same as that of the input signal. As a result, the controller can adjust the frequency, amplitude and offset of the output signal separately.

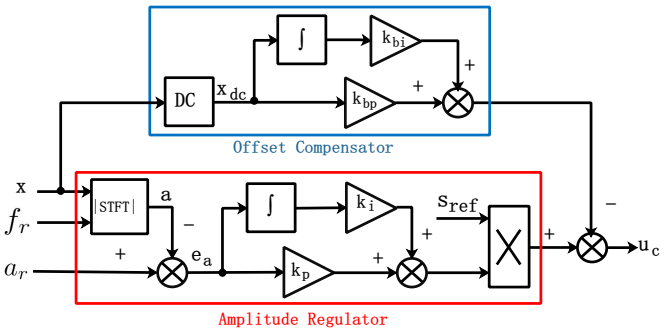

Fig. 7: Direct amplitude controller

Fig. 7 shows the structure of such controller. The controller takes the desired amplitude, desired frequency and feedback position signal as inputs, it outputs the voltage signal applied to the motor. There are two modules in the controller, namely, amplitude regulator module, and offset compensator module. Different from traditional PI control that directly takes the error of position in real time as input, the amplitude regulator module of the proposed controller applies short time Fourier transform (STFT) to the feedback position signal to obtain the amplitude of it at first. Then, it is the error of amplitude rather than error of position being sent to a built-in PI controller. In addition, different from traditional PI control that directly applies its output to the plant under control, the built-in PI controller in amplitude regulator module uses its output to modulate the amplitude of a sinusoidal signal applies to the plant under control. The controller output u_c in time domain can be expressed as:

$$u_c = \left(k_p \cdot e_a + k_i \cdot \int_0^t e_a \cdot dt\right) \cdot s_{ref} - k_{pb} \cdot x_{dc} - k_{ib} \cdot \int_0^t x_{dc} \cdot dt \tag{15}$$

where

$$\begin{cases} s_{ref} = sin(2\pi \cdot f_r \cdot t) \\ e_a = a_r - a \\ a = \left| \left(\int_{-\infty}^{+\infty} w\left(t-\tau\right) x\left(\tau\right) e^{-j \cdot 2\pi f_r \tau} d\tau \right) \right| \\ x_{dc} = \left(\int_{-\infty}^{+\infty} w\left(t-\tau\right) x\left(\tau\right) d\tau \right) \end{cases} \tag{16}$$

f_r is the desired frequency of output position signal. e_a is the error of amplitude. a_r is the desired amplitude of position signal x based on STFT. x_{dc} is the windowed DC component in output position signal. k_p and k_i are proportional gain and integral gain of amplitude regulator module. k_{pb} and k_{pi} are proportional gain and integral gain of offset regulator module. In implementation, a is obtained by taking the modulus of the short time Fourier transform of the output signal.

$$a\left(t\right) = \left| \int_{t-\frac{1}{f_r}}^{t} w^{TS}\left(t-\tau\right) x\left(\tau\right) e^{-j \cdot 2\pi f_r \tau} d\tau \right| \tag{17}$$

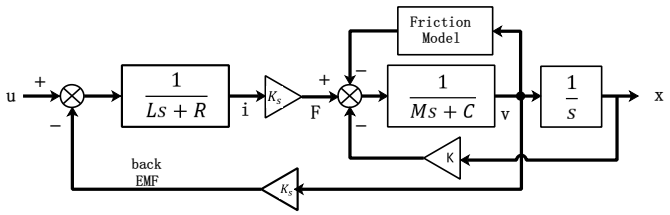

(a) Block diagram of HFRR including friction

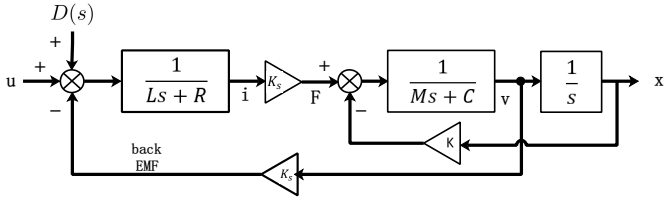

(b) Modified block diagram of HFRR including friction

Fig. 8: Modification on the model of HFRR including friction: the friction can be transferred to act on HFRR via the same channel as control input (shown as $D(s)$ in (b)).

where, the time-shifted Hamming window $w^{TS}(t)$ is:

$$w^{TS}(t) = 0.54 - 0.46cos(2\pi f_r t), 0 \le t \le \frac{1}{f_r} \tag{18}$$

D. Convergence Analysis

The denominator of the transfer function of HFRR without friction is:

$$\begin{aligned} P(s) = LM \cdot s^3 + (LC + RM) \cdot s^2 + \\ \left(K_s^2 + RC + Lk\right) \cdot s + Rk \end{aligned} \tag{19}$$

Therefore, the characteristic equation of HFRR transfer function without friction is:

$$P(s) = 0 \tag{20}$$

Substitute the values listed in the Table. I into (20), we can obtain:

$$0.0021s^3 + 2.8893s^2 + 594.3656s + 10584 = 0 \tag{21}$$

The poles of the HFRR transfer function are:

$$\begin{aligned} p_1 &\approx -19.65964 < 0 \\ p_2 &\approx -225.87700 < 0 \\ p_3 &\approx -1157.17522 < 0 \end{aligned}$$

Remark III.1: HFRR as a system without friction is open loop stable.

The proposed controller in s domain can be expressed as:

$$C(s) = \left[(k_p + \frac{k_i}{s}) * \frac{\omega_r}{s^2 + \omega_r^2}\right] \cdot E_a(s) - (k_{pb} + \frac{k_{ib}}{s}) \cdot X_{dc}(s) \tag{22}$$

where $*$ indicate convolution and $\omega_r = 2\pi f_r$. Hence:

$$C(s) = \frac{k_i \omega_r}{s^2 + \omega_r^2} \cdot E_a(s) - (k_{pb} + \frac{k_{ib}}{s}) \cdot X_{dc}(s) \tag{23}$$

Assumption 1: the friction as a disturbance is differentiable and bounded. Then it satisfies matching condition, where the disturbance can be transferred to act on the system via the same channel as control input [26].

Fig. 8.(a) shows the block diagram of HFRR considering friction. Once the matching condition is fulfilled, the friction as disturbance can be transferred to an equivalent input disturbance $D(s)$ as shown in. Fig. 8.(b). Therefore, the output of the closed loop system in frequency domain can be expressed as:

$$\begin{aligned} X(s) = G(s) \cdot \left[\frac{k_i \omega_r}{s^2 + \omega_r^2} \cdot E_a(s) - (k_{pb} + \frac{k_{ib}}{s}) \cdot X_{dc}(s)\right] \\ + G(s) \cdot D(s) \end{aligned} \tag{24}$$

where the plant model $G(s)$ and equivalent input disturbance $D(s)$ are given as:

$$\begin{cases} G(s) &= \frac{K_s}{P(s)} \\ D(s) &= -\frac{(L \cdot s + R)}{K_s} \cdot F_f(s) \end{cases} \tag{25}$$

The output of the closed loop system can be decomposed into sinusoidal component $X_{ac}(s)$ and generalised output disturbance $X_{dis}(s)$ as:

$$X(s) = X_{ac}(s) + X_{dis}(s) \tag{26}$$

where

$$\begin{cases} X_{ac}(s) &= G(s) \cdot \frac{k_i \omega_r}{s^2 + \omega_r^2} \cdot E_a(s) \\ X_{dis}(s) &= G(s) \cdot \left[D(s) - (k_{pb} + \frac{k_{ib}}{s}) \cdot X_{dc}(s)\right] \end{cases} \tag{27}$$

Assumption 2: perfect knowledge of $a(t)$ and $x_{dc}(t)$ can be obtained. Then, $e_a(t)$ can be approximated as error of amplitude in real time. In addition, $x_{dc}(t)$ is nonzero for only DC component in output signal.

As the disturbance is assumed to be bounded and $x_{dc}(t) = 0$ for sinusoidal component of the output signal, the amplitude of the component of the output signal at the desired angular frequency $\omega_r = 2\pi f_r$ at steady state can be expressed as:

$$\begin{aligned} |X(j\omega_r)| &= |X_{ac}(j\omega_r) + X_{dis}(j\omega_r)| \\ &= |G(j\omega_r) \cdot \frac{k_i \omega_r}{s^2 + \omega_r^2} \cdot E_a(j\omega_r) + G(j\omega_r) \cdot D(j\omega_r)| \\ &= |G(j\omega_r) \cdot \left(\frac{k_i \omega_r}{s^2 + \omega_r^2} \cdot E_a(j\omega_r) + D(j\omega_r)\right)| \\ &= |G(j\omega_r)| \cdot [k_i \cdot (a_r - |X(j\omega_r)|) + \Delta] \end{aligned} \tag{28}$$

where Δ represents the equivalent uncertainty of the control input of HFRR due to friction. Rearrange the last line of (28),we have:

$$|X(j\omega_r)| = \frac{|G(j\omega_r)| \cdot k_i}{1 + |G(j\omega_r)| \cdot k_i} \cdot (a_r + \frac{\Delta}{k_i}) \tag{29}$$

Remark III.2: At steady state, arbitrarily small error of amplitude at the desired frequency can be achieved by choosing $k_i \gg 1$. And we have:

$$\lim_{k_i \to \infty} |X(j\omega_r)| = a_r \tag{30}$$

Parameter	Symbol(unit)	Value
Coil resistance	R(Ω)	5.4
Coil inductance	L(H)	3.86×10^{-3}
Mass of moving components	M(Kg)	0.512
Motor constant	K_s(N/A)	24
Spring stiffness	k(N/m)	1960
Damping coefficient	C($n.s.m^{-1}$)	2
Asperity stiffness	σ_0 (N/m)	10^5
Damping coefficient	σ_1 (Ns/m)	$10^{\frac{1}{2}}$
Viscous coefficient	σ_2 (Ns/m)	0.4
Coulomb friction	F_c (N)	46.49
Stiction force	F_s (N)	55.3
Stribeck velocity	v_s (m/s)	0.001
Shape factor	σ_{vs} (-)	2

TABLE I: Values of parameters used in simulation

Parameter	Value
DC Bus Voltage	$42V$
DSP Clock Frequency	$2 \times 10^8 Hz$
PWM frequency	$4 \times 10^4 Hz$
Encoder Resolution	$5 \times 10^{-7} m$

TABLE II: Parameters of experimental platform

Considering the DC component of the output signal at steady state, we have:

$$\begin{aligned} X(j0) &= X_{ac}(j0) + X_{dis}(j0) \\ &= 0 + X_{dis}(j0) \\ &= G(j0) \cdot \left[D(j0) - (k_{pb} + \frac{k_{ib}}{j0}) \cdot X_{dc}(j0) \right] \end{aligned} \tag{31}$$

Remark III.3: At steady state, the DC component of the output signal $X(j0) \to 0$.

As a result, the system is open loop stable. By assuming the fulfilment of matching condition and perfect knowledge of amplitude and DC offset, it can be proved that arbitrarily small error of amplitude of the closed loop system at the desired frequency can be achieved at steady state. In addition, the DC offset of the position signal of the closed loop system approaches zero at steady state.

IV. Simulations and Experiments

A. Simulations

In simulation, the desired amplitude of vibration at 50Hz is set as 200um. Table. I gives the values of the parameters applied in simulation. Fig. 9 shows the simulated amplitudes of position signals using different controllers. It is assumed that the shaft of VCM is at standstill initially. It can be found that the amplitude of position signal using the proposed controller converges to the desired value. There is steady state error of amplitude exists for PI controller, which is in agreement with [24]. In addition, when applying PR controller to HFRR, the closed loop system become unstable.

By ignoring the effect of frictional load, the transfer function of the closed loop system under no load condition using PR control can be obtained. Fig. 10 shows the root locus plot of the closed loop system using proportional control. The gain

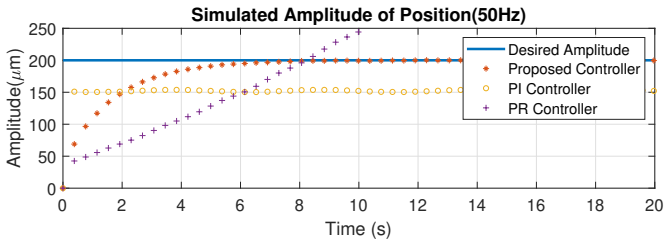

Fig. 9: Simulated amplitudes of position signals using different controllers

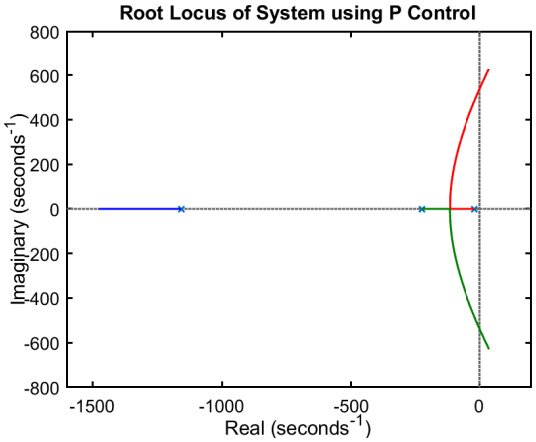

Fig. 10: Root locus plot of the closed loop system using proportional control

varies from 0 to 5×10^4. The corresponding loop transfer function is given by:

$$L_p(s) = \frac{K_p K_i}{P(s) + K_p K_s} \tag{32}$$

By applying Routh's stability criterion, the closed loop system is stable when $K_p < 33639.48796$. Let $K_p = 10$, the loop transfer function of the closed loop system using proportional resonant control can be expressed as:

$$L_{pr}(s) = \frac{K_s}{P(s)} \cdot \frac{K_p \cdot s^2 + K_i \cdot s + K_p \cdot \omega_0^2}{s^2 + \omega_0^2} \tag{33}$$

Fig. 11 shows the root locus plot of the closed loop system using proportional resonant control with $K_p = 10$, $\omega_0 = 100\pi$. The gain varies from 0 to 5×10^4. By applying Routh's stability criterion, it is found that there is no positive resonant gain that lead to stable system. Fig. 12 shows the magnified view of Fig. 11, which clearly shows the conjugate pole pairs on the right hand side of imaginary axis [27].

B. Experiment Setup

The setup of the experimental platform applied in research is shown in Fig. 13. A digital signal processor is used to implement the controller, which reads in the position, normal force and friction signals from the sensors on HFRR. A full bridge inverter is used to alternate the voltage applied to the terminals of VCM. The inverter is controlled by digital signal processor through pulse width modulation technique. A PC is

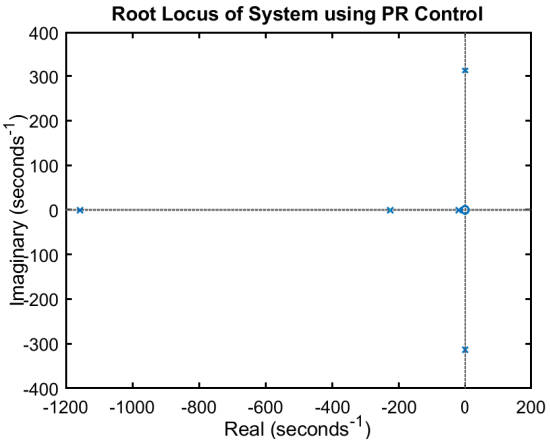

Fig. 11: Root locus plot of the closed loop system using proportional resonant control with $K_p = 10$ (K_i is varying)

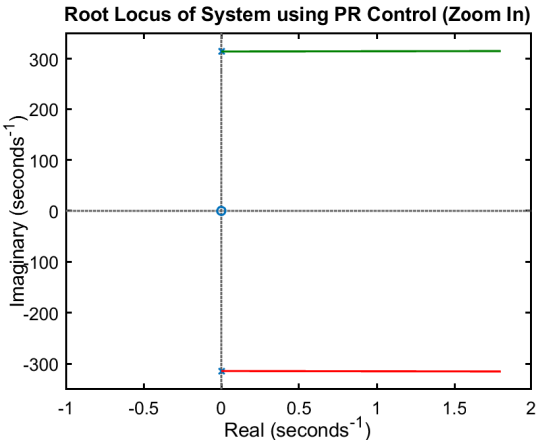

Fig. 12: Root locus plot of the closed loop system using proportional resonant control with $K_p = 10$ (K_i is varying) (Zoom In)

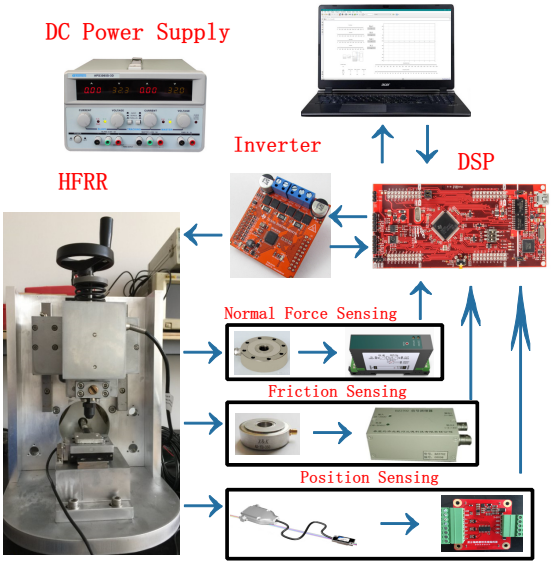

Fig. 13: Configurations of experimental platform

Frequency(Hz)	Amplitude(μm)
30Hz	100μm
30Hz	150μm
30Hz	200μm
30Hz	250μm
40Hz	100μm
40Hz	150μm
40Hz	200μm
40Hz	250μm
50Hz	100μm
50Hz	150μm
50Hz	200μm
50Hz	250μm
60Hz	100μm
60Hz	150μm
60Hz	200μm
60Hz	250μm

TABLE III: Experimental conditions

used to achieve signals monitoring in real time. In Fig. 13, an incremental encoder in position sensing module is used to measure the position of the shaft of VCM, of which the resolution is 0.5μm. In addition, A load cell connected with an isolated voltage transducer form the normal force sensing module, which is used to measure the normal force exerted on the specimen during experiment. The conditioned normal force signal passing through isolated voltage transducer is feed into digital signal processor. Similarly, a piezoelectric sensor together with charge amplifier compose the friction sensing module, of which the output is feed into digital signal processor through AD. The digital signal processor applied to experimental platform is equipped with a 32-bit floating point CPU, which provides 200 MHz of signal processing performance. The parameters of digital controller, full bridge inverter and incremental encoder on experimental platform are presented inTable. II.In addition, the parameters of VCM on experimental platform are listed in Table. I.

To conduct the experiments, the test ball and the test plate with lubricant covered on top should be mounted on HFRR properly in the first place. Secondly, the auxiliary power supplies should be turned on to allow the adjustment of normal force exerts on the specimen and the initialisation of both programs running in DSP and host PC. Thirdly, the main power supply should be turned on to enable the operation of the inverter by DSP. Finally, the oscillation of VCM on HFRR is activated. To simplify the experiments, we keep the types of specimen and values of normal force constant in each test. The settings of remaining experimental conditions applied in experiments are shown in Table. III.

Remark IV.1: The position counter register of the digital signal processor on the experimental platform will always be set to a predefined initial value on index events during each cyclic period of oscillation to mitigate potential drift problem [28] [29].

In Table III, there are 16 sets of experimental conditions. The frequency varies from 30Hz to 60Hz. The amplitude varies from 100μm to 250μm. The specimens in all experiments are chosen as aluminium plate with petroleum ether (Al&PE) covered on top of them. To make sure the initial conditions

Frequency(Hz)	Amplitude(μm)	Specimen	Normal Force(N)
30Hz	$100\mu m$	Al&PE	6N

TABLE IV: Experimental Conditions for Controllers Tuning

such as surface roughness are same in each experiment, both aluminium plate and petroleum ether between contacting surfaces should be replaced at the end of each test. To assess the performance of the proposed control method, comparisons among conventional PI control, PR control and the proposed control method have been done. The parameters for each controller are tuned under the condition shown in Table. IV, and then keep constant in remaining tests.

C. Discussion on Discretisation Procedure

To implement the aforementioned controller using digital signal processor, it is required that the continuous time controller should be discretised. The output from a discrete time controller is piece-wise constant over the sampling interval in this case:

$$u = u(nT), \quad nT \leq t < (n+1)T \tag{34}$$

Where T is sampling period.

For a continuous system with frequency function $G(i\omega)$, when the input of the continuous system is constant over the sampling interval, the corresponding frequency function for the sampled system is given by $G_T(e^{i\omega T})$. The relationship between them can be described by:

$$\left|G(i\omega) - G_T\left(e^{i\omega T}\right)\right| \leq \omega T \cdot \int_0^\infty |g(\tau)| d\tau \tag{35}$$

where $g(\tau)$ is the impulse response of $G(s)$. As a rule of thumb, the difference between two frequency functions can be regarded as small when the frequency is less than one tenth of the sampling frequency: [30]

$$\omega < \frac{2\pi}{10T} \tag{36}$$

In experiments, the frequency of PWM by digital signal processor has been set as $40kHz$. In addition, the control algorithm has been set to be executed 1×10^4 times per second. Therefore, the dominated sampling time is $T = 1 \times 10^{-4}s$ for the discrete time controller. The desired frequency of the output position of HFRR in our research is less than $70Hz$. Hence:

$$\omega < 2\pi \times 70 < \frac{2\pi}{10 \times T} \tag{37}$$

The frequency of interest for HFRR is less than one tenth of the sampling frequency of the discrete time controller. As a result, the difference between the continuous system in analysis and sampled system in experiment can be considered as small.

D. Experiment Results

Fig. 14 shows the amplitudes of position signals using PR controller at different frequencies. The desired amplitude is set as $200\mu m$. It can be found that the amplitudes of

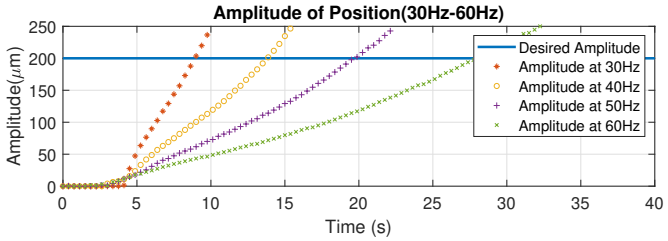

Fig. 14: Amplitudes of experimental position signals at different frequencies using PR control

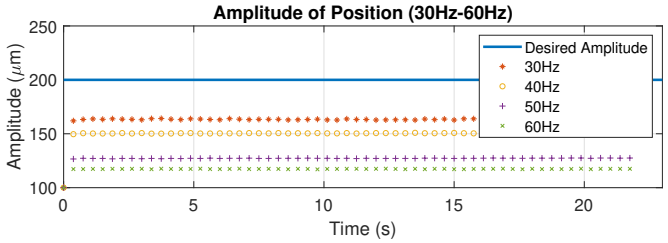

Fig. 15: Amplitude of experimental position signals at different frequencies using PI control

position signals corresponding to each frequency always keep increasing, which indicates an unstable system.

Fig. 15 and Fig. 16 are the amplitudes of position signals acquired in experiments using PI and the proposed controllers. The desired values of amplitude are all set as $200um$. It can be found that the performance of the conventional PI control in terms of amplitude degrades significantly as frequency increases. However, the proposed control method shows the ability of amplitude keeping at different frequencies. Fig. 17 and Fig. 18 are the position signals acquired in experiments using PI and the proposed controllers. The desired values of amplitude are all set as $200\mu m$. Fig. 19 shows the friction signals acquired from experiments. There are harmonic components appear, which is in agreement with the results in [31]. In addition, the normal force is changed to 10N when obtaining Fig.20. It can be found that the convergence of amplitude error can still be guaranteed.

It can be found that the magnitude of relative error increases at higher frequency using conventional PI control. The relative errors of amplitudes given by the proposed control method all converge to zero at different frequencies. The rate of convergence depends on the frequency of vibration. Fig. 21 are the outputs of PI controller and the proposed controller at 30Hz with the desired amplitude of $200\mu m$. The control efforts are similar.

Fig. 22 and Fig. 23 show the relative errors of amplitude for both conventional PI controller and the proposed controller at steady states. The proposed control outperforms the conventional PI control significantly in terms of amplitude keeping. The relative errors of amplitude using the proposed controller are less than 0.5% in all 16 experiments. The conventional PI controller presents higher relative error as either amplitude or frequency increasing. At 60Hz, the relative error of amplitude can be as large as 80%. On the contrary, the relative error of amplitude using the proposed controller

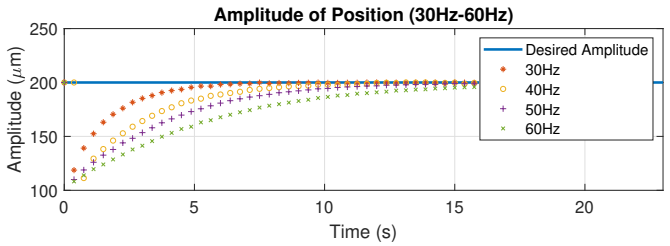

Fig. 16: Amplitude of experimental position signals at different frequencies using the proposed control method

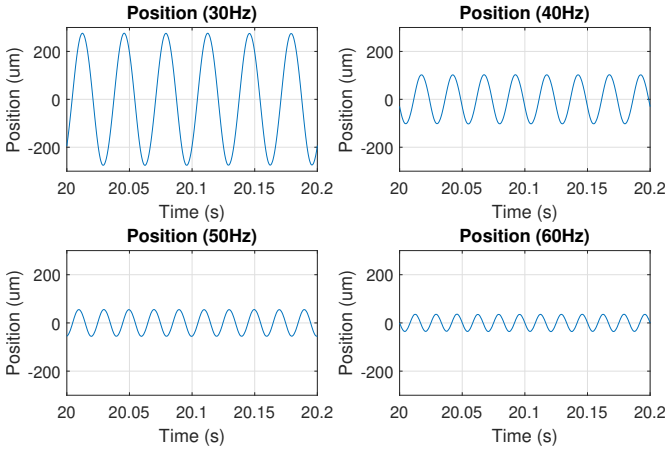

Fig. 17: Experimental position signals at different frequencies using PI control

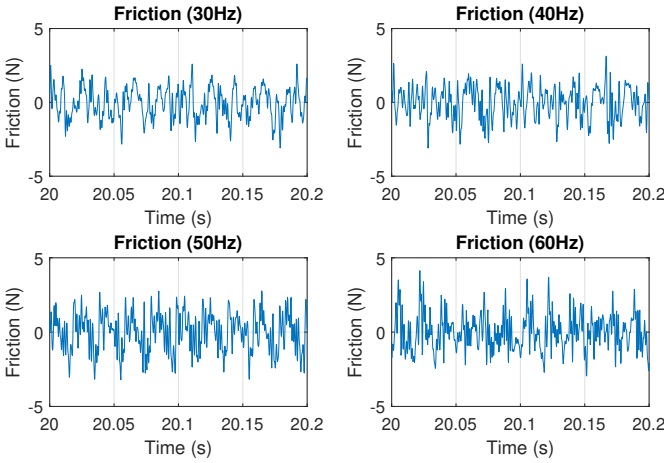

Fig. 19: Friction signal acquired from experiments

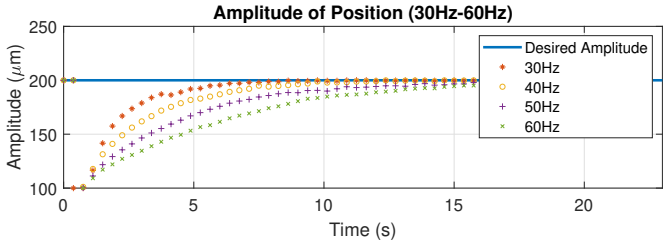

Fig. 20: Amplitude of experimental position signals at different frequencies using the proposed control method with 10N normal force

decreases as either amplitude or frequency increasing. This implies that the proposed control algorithm is attractive for application of vibration control in high frequency band. In both situations, the relative offsets are always less than 1%, which is of little difference.

Fig. 24 and Fig. 25 show the total harmonic distortions (THD) of position signals at steady states under different conditions. THD applied in the analysis is determined from the fundamental frequency of vibration and the first three harmonics of position signal acquired from corresponding

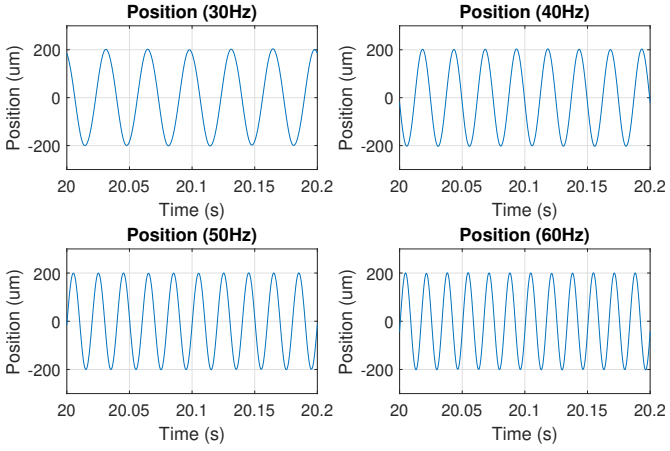

Fig. 18: Experimental position signals at different frequencies using the proposed control method

test. This is used to assess the frequency keeping ability of control algorithm. At 30Hz, THD of position signal using conventional PI control is less than that using the proposed controller. However, at higher frequencies, the performance of proposed control in terms of harmonics suppression is better than that of conventional control. This observation agrees with the conclusion that the proposed control algorithm is attractive for application of vibration control in high frequency band in tribotests.

Remark IV.2: In addition, as VCM is also applied to the design of electrodynamic shaker in vibration test systems, the proposed control method can be applied to the regulation of the amplitude of acceleration of the shaker in vibration tests, where the encoder is replaced by accelerometer [32] [33].

V. Conclusion

Direct amplitude control is proposed to deal with the amplitude keeping problem of high frequency reciprocating rig subjects to frictional load. The proposed control scheme consists of an amplitude regulator and an offset compensator. It takes the error of the amplitude of the position signal as performance index. The analysis shows that the error of amplitude of position signal of the closed loop system converges to zero by applying the proposed control. A digital signal processor based experimental platform is built to verify the proposed control method. Both PI control and PR control are introduced to experiments for the purpose of comparison.

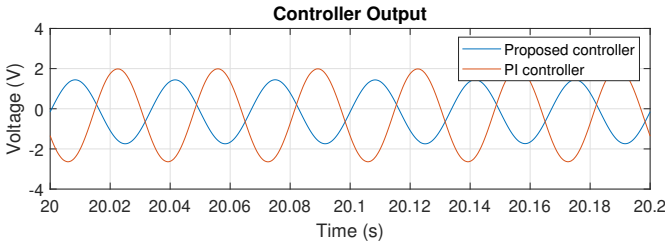

Fig. 21: PI and the proposed controllers outputs at 30Hz

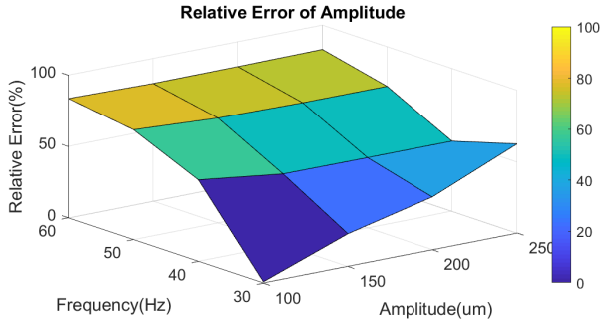

Fig. 22: Relative errors of amplitude using PI control under different conditions

Although PR control has been widely applied in the application of tracking sinusoidal reference signal, it leads to an unstable system due to the large phase delay of voice coil motor based high frequency reciprocating rig at high frequency band. It is found that the proposed direct amplitude control outperforms PI control in terms of amplitude keeping and harmonics suppression in high frequency reciprocating motion.

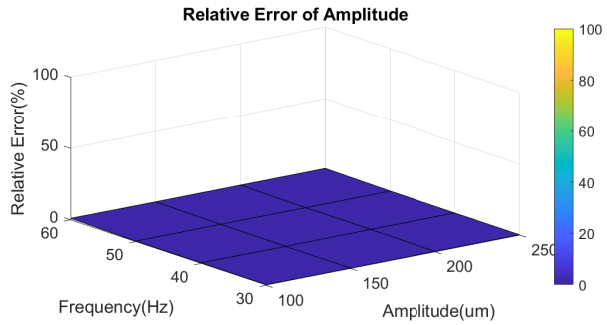

Fig. 23: Relative errors of amplitude using the proposed control under different conditions

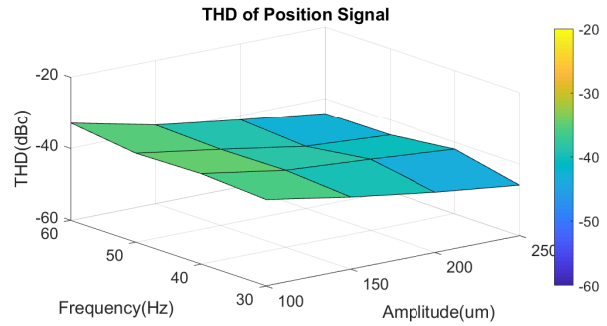

Fig. 24: Total harmonic distortions of position signals using PI control under different conditions

REFERENCES

[1] K. G. Budinski, *Guide to Friction, Wear and Erosion Testing*. 100 Barr Harbor Drive, PO Box C700, West Conshohocken: ASTM International, 2007.

[2] B. Bhushan, *Introduction to Tribology*. John Wiley & Sons Ltd, The Atrium, Southern Gate, Chichester, West Sussex, PO19 8SQ, United Kingdom: A John Wiley & Sons, Ltd., 2013.

[3] ——, *Modern Tribology Handbook*, 1st ed. USA: CRC pree LLC, December 2000, vol. 1.

[4] S. Wu, Z. Jiao, L. Yan, R. Zhang, J. Yu, and C. Chen, "Development of a direct-drive servo valve with high-frequency voice coil motor and advanced digital controller," *IEEE/ASME Transactions on Mechatronics*, vol. 19, no. 3, pp. 932–942, June 2014.

[5] E. Csencsics, M. Thier, R. Hainisch, and G. Schitter, "System and control design of a voice coil actuated mechanically decoupling two-body vibration isolation system," *IEEE/ASME Transactions on Mechatronics*, vol. 23, no. 1, pp. 321–330, Feb 2018.

[6] E. Asadi, A. Khajepour, and M. B. Khamesee, "A new low-profile electromagnetic-pneumatic actuator for high-bandwidth applications," *IEEE/ASME Transactions on Mechatronics*, vol. 23, no. 5, pp. 2207–2217, Oct 2018.

[7] *Diesel fuel-Assessment of lubricity using the high frequency reciprocating rig (HFRR)*, British Standards Institution Std. 12 156-1:2016, 2016.

[8] A. Maddahi, N. Sepehri, and W. Kinsner, "Fractional-order control of hydraulically powered actuators: Controller design and experimental validation," *IEEE/ASME Transactions on Mechatronics*, vol. 24, no. 2, pp. 796–807, April 2019.

[9] X. Hu, L. Cao, Y. Luo, A. Chen, E. Zhang, and W. J. Zhang, "A novel methodology for comprehensive modeling of the kinetic behavior of steerable catheters," *IEEE/ASME Transactions on Mechatronics*, vol. 24, no. 4, pp. 1785–1797, Aug 2019.

[10] H. Yu, T. Chen, and C. Liu, "Adaptive fuzzy logic proportional-integral-derivative control for a miniature autofocus voice coil motor actuator with retaining force," *IEEE Transactions on Magnetics*, vol. 50, no. 11, pp. 1–4, Nov 2014.

[11] J. . Seok and S. . Kim, "Vcm controller design with enhanced disturbance decoupling for precise automated manufacturing processes," *IET Electric Power Applications*, vol. 6, no. 8, pp. 575–582, Sep. 2012.

[12] H. Guo, D. Wang, and J. Xu, "Research on a high-frequency response direct drive valve system based on voice coil motor," *IEEE Transactions on Power Electronics*, vol. 28, no. 5, pp. 2483–2492, May 2013.

[13] Y. Gao, "Active disturbance-rejection control of voice coil motor based on rbf neural network," in *2011 International Conference on Consumer Electronics, Communications and Networks (CECNet)*, April 2011, pp. 3895–3898.

[14] L.Xing and H.Zhou, "Research and application of voice coil actuator," *Micromotors*, 2011.

[15] S.Huang and Z.Feng, "Parameter self-optimizing pid control for linear motor of the mf type," *Aviation Precision Manufacturing Technology*, vol. 14, no. 5, Oct 2005.

[16] T. Piatkowski, "Dahl and lugre dynamic friction models-the analysis of selected properties," *Mechanism and Machine Theory*, vol. 73, pp. 91 – 100, 2014.

[17] P. Korondi, *Robot Applications*. 4-6 Bertalan Lajos Street, Budapest 1111, Hungary: BME-MOGI, 2014.

[18] W. Rong, S. Liang, L. Wang, S. Zhang, and W. Zhang, "Model and control of a compact long-travel accurate-manipulation platform," *IEEE/ASME Transactions on Mechatronics*, vol. 22, no. 1, pp. 402–411, Feb 2017.

[19] T. Zhang, M. Tran, and H. Huang, "Admittance shaping-based assistive control of sea-driven robotic hip exoskeleton," *IEEE/ASME Transactions on Mechatronics*, vol. 24, no. 4, pp. 1508–1519, Aug 2019.

[20] C. C. de Wit, H. Olsson, K. J. Astrom, and P. Lischinsky, "A new model for control of systems with friction," *IEEE Transactions on Automatic Control*, vol. 40, no. 3, pp. 419–425, Mar 1995.

[21] S. Huang, W. Liang, and K. K. Tan, "Intelligent friction compensation: A review," *IEEE/ASME Transactions on Mechatronics*, vol. 24, no. 4, pp. 1763–1774, Aug 2019.

[22] D. Aslan and Y. Altintas, "Prediction of cutting forces in five-axis

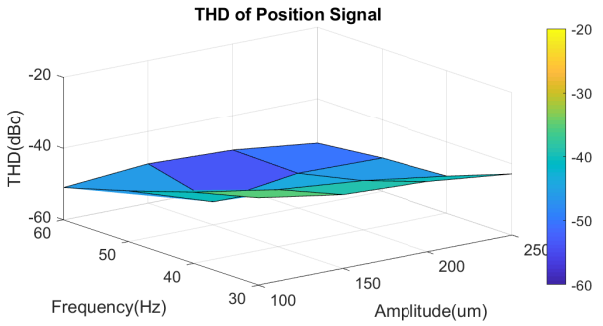

Fig. 25: Total harmonic distortions of position signals using the proposed control under different conditions

milling using feed drive current measurements," *IEEE/ASME Transactions on Mechatronics*, vol. 23, no. 2, pp. 833–844, April 2018.

[23] A. Yuen and Y. Altintas, "Constrained trajectory generation and control for a 9-axis micromachining center with four redundant axes," *IEEE/ASME Transactions on Mechatronics*, vol. 23, no. 1, pp. 402–412, Feb 2018.

[24] D. N. Zmood and D. G. Holmes, "Stationary frame current regulation of pwm inverters with zero steady-state error," *IEEE Transactions on Power Electronics*, vol. 18, no. 3, pp. 814–822, May 2003.

[25] S. Fukuda and T. Yoda, "A novel current-tracking method for active filters based on a sinusoidal internal model [for pwm invertors]," *IEEE Transactions on Industry Applications*, vol. 37, no. 3, pp. 888–895, May 2001.

[26] S. Li, J. Yang, W. Chen, and X. Chen, *Disturbance Observer Based Control Methods and Applications*. 6000 Broken Sound Parkway NW, Suite 300 Boca Raton: CRC Press, Taylor & Francis Group, 2016.

[27] S. C. Kuo, *Automatic Control Systems*. Upper Saddle River, NJ, USA: Prentice Hall, 1975.

[28] *TMS320F2837xD Dual-Core Delfino Microcontrollers Technical Reference Manual*, Texas Instruments, 12 2017.

[29] *Mercury II 1600 The Next Generation of High Performance Encoders*, MicroE System, 2011, rev. i.

[30] T. Glad and L. Ljung, *Control Theory Multivariable and Nonlinear Methods*. 29 West 35th Street, New York, NY, 10001: Taylor & Francis Group, 2000.

[31] P. Rehbein and J. Wallaschek, "Friction and wear behaviour of polymer/steel and alumina/alumina under high-frequency fretting conditions," *Wear*, vol. 216, no. 2, pp. 97 – 105, 1998.

[32] L. D. Flora and H. A. Grundling, "Time domain sinusoidal acceleration controller for an electrodynamic shaker," *IET Control Theory Applications*, vol. 2, no. 12, pp. 1044–1053, December 2008.

[33] K. Rana, "Fuzzy control of an electrodynamic shaker for automotive and aerospace vibration testing," *Expert Systems with Applications*, vol. 38, no. 9, pp. 11 335 – 11 346, 2011. [Online]. Available: http://www.sciencedirect.com/science/article/pii/S0957417411004088

Ruotong Wang received the B.Eng. degree in electronics communication and engineering from University of Liverpool, U.K., in 2014 and M.Sc. degree in communication and signal processing from Imperial College London, U.K., in 2016. He is currently pursuing Ph.D. degree in the University of Liverpool, U.K. His current research interests include the control of voice coil motor and its applications in tribotest.

Xin Yin received the B.Eng. degree in electrical and electronic engineering from the University of Sheffield, U.K., in 2008 and M.Sc. degree in telecommunication from University College London, U.K., in 2009, and the Ph.D. degree in electrical and electronic engineering from the University of Manchester, U.K., in 2016. He is presently working as a research associate of the control and optimization of microgrid with the University of Liverpool. His current research interests include control and optimization of smart grid with the energy storage system, renewable energy generation and integration and demand side response.

Qibing Wang He is currently pursuing Ph.D. degree in mechanical engineering from Tianjin University, China. He is a Fellow of the Institution of Engineering and Technology, U.K. He is also the director of Zhejiang Sicher Elevator Science and Technology Institute, China. His research interests include design and manufacturing of smart mechatronics, and automation.

Lin Jiang (M-00) received the B.S. and M.S. degrees from Huazhong University of Science and Technology (HUST), China, in 1992 and 1996; and the Ph.D. degree from the University of Liverpool, UK, in 2001, all in Electrical Engineering. He worked as a Postdoctoral Research Assistant in the University of Liverpool from 2001 to 2003, and Postdoctoral Research Associate in the Department of Automatic Control an Systems Engineering, the University of Sheffield from 2003 to 2005. He was a Senior Lecturer at the University of Glamorgam from 2005 to 2007 and moved to the University of Liverpool in 2007. Currently, he is a Reader in The University of Liverpool. His current research interests include control and analysis of power system, smart grid, and renewable energy.